Journal of Materials Chemistry B

Facile Synthesis of Three-Dimensional Hydroxyapatite Monolith for Protein Adsorption

Journal:	*Journal of Materials Chemistry B*
Manuscript ID	TB-ART-09-2021-002021.R1
Article Type:	Paper
Date Submitted by the Author:	25-Oct-2021
Complete List of Authors:	Lyu, Yanting; Osaka University, Asoh, Taka-Aki; Osaka University, Applied Chemistry Uyama, Hiroshi; Osaka Univerisity,

ARTICLE

Facile Synthesis of Three-Dimensional Hydroxyapatite Monolith for Protein Adsorption

Received 00th January 20xx,
Accepted 00th January 20xx

DOI: 10.1039/x0xx00000x

Yanting Lyu, [a] Taka-Aki Asoh *[a] and Hiroshi Uyama *[a]

Hydroxyapatite (HA) shows promising applications in the clinical treatment of bone defects owing to its excellent physicochemical properties, such as biocompatibility, bioactivity, and osteoconductivity. However, it is difficult to maintain a porous structure in HA materials because of processing difficulties. In this study, a hard template method was developed to prepare a porous HA monolith with a hierarchical pore structure and high porosity. The cellulose monolith template was prepared from cellulose acetate using a thermally induced phase separation method. The cellulose monoliths were then immersed into the HA slurry to form a cellulose_HA composite monolith, which was converted to an HA monolith by burning in air to remove the cellulose monolith. Owing to the hierarchically porous structure of the cellulose monolith template, the obtained HA monolith demonstrated a hierarchically porous structure. Furthermore, the HA monolith was explored to study the adsorption and release properties of bovine serum albumin (BSA), which indicated that the HA monolith had a high adsorption capacity (388.6 mg/g) and sustained release from the BSA-loaded HA monolith. Thus, HA monoliths have potential applications in the field of protein purification and biomaterials.

Introduction

Hydroxyapatite ($Ca_{10}(PO_4)_6(OH)_2$, HA) is the main mineral component in the hard tissue of vertebrate bones and teeth as well as the most stable calcium phosphate phase under physiological conditions.[1, 2] Owing to its excellent physicochemical properties, such as biocompatibility,[3] bioactivity,[4] and osteoconductivity,[5] synthetic HA shows promising applications in bone repair,[6] tissue engineering,[7] drug/protein/gene delivery,[8-10] and other biomedical fields.[11] However, HA materials exhibit poor cell crawling and cell adhesion, slow replacement, and difficult ingrowth, thereby limiting the clinical application of HA materials.[12] This is because they fail to provide a microenvironment suitable for bone growth, which should be a highly interconnected three-dimensional hierarchical structure with macropores and micronano structures.[13] HA-polymer composites are potential candidates for solving these problems. For example, HA/starch composites,[14] HA/cellulose,[15] and HA/cellulose triacetate nanofibers[10] were prepared for protein adsorption and biomedical bone substitution. The improved properties of such materials result from the combination of the compressive strength of the inorganic ceramic phase and the toughness and flexibility of the polymer.[16] However, there is still a high demand for the development of a pure HA that can cater to applications that require unique structures and specific properties.

Department of Applied Chemistry, Graduate School of Engineering, Osaka University, 2-1 Yamadaoka, Suita, Osaka 565-0871, Japan.
E-mail: asoh@chem.eng.osaka-u.ac.jp, uyama@chem.eng.osaka-u.ac.jp
DOI: 10.1039/x0xx00000x

Hierarchically porous materials have received considerable attention in biomedical and environmental applications owing to their high surface area, high pore volume ratios, excellent accessibility to active sites, and enhanced mass transport and diffusion.[17-20] Compared to conventional porous materials with uniform pore dimensions, hierarchical porous materials with well-defined pore dimensions and topologies can offer the combined benefits of each pore size in a single structure. For example, micro-/mesopores possess size or shape selectivity and a high surface area for active site dispersion. The macropores act as flow-through channels, can minimize diffusive resistance to mass transport, and can provide easier access to the active sites.[17, 21]

Such novel interconnected porous HA materials with a three-dimensional network can induce early osteogenesis from the surrounding cells and tissues through cell adhesion, penetration, proliferation, and tissue ingrowth.[22] For these reasons, hierarchically porous monolithic HA materials are potential candidates for biomaterial applications. Hierarchically porous monolithic HA materials with controlled morphology, porosity, and architecture (especially with hierarchical porosity and mesopores in combination with macropores or micropores) are highly desirable owing to their unique structural features. Various methods are currently available for the preparation of hierarchical structures, such as sintering,[23] freeze-casting,[24] and 3D printing.[7] The most commonly used synthetic technique for the fabrication of inorganic materials is hard templating, in which a hierarchical structured polymer is used as a template, followed by carbonization of the composite and subsequent removal of the template.[6, 25, 26]

Cellulose monoliths, as a result of their monolithic and hierarchically porous structure, possess several features, such

as hydrophilicity, easy chemical modification, large surface area, insolubility in water and common organic solvents, and high mechanical strength.[27] Additionally, hierarchically porous cellulose monoliths exhibiting high hydrophilicity and tolerance toward common solvents can be easily fabricated from a cellulose acetate solution by thermally induced phase separation (TIPS).[28] Moreover, HA nanopowders with unsaturated atoms can effectively interact with cellulose;[15] the Ca ions and –OH groups of HA can interact with the $–NH_2$ or –OH groups of chitosan to form a homogenous HA slurry.[29] Utilizing the hydrophilic but water-insoluble properties of cellulose monoliths, it is possible to incorporate HA nanopowders or HA slurry into the monolith skeleton.

Herein, we used an eco-friendly cellulose monolith as a template to prepare a hierarchically porous HA monolith. The cellulose_HA composite monolith was prepared in the presence of a cellulose monolith and commercial HA powder as raw materials. Finally, the HA monolith was obtained by burning the composite monolith in air to remove the cellulose template. Owing to the hierarchically porous structure of the cellulose monolith template, the obtained HA monolith showed a hierarchically porous structure. Moreover, the pore structures could be controlled by altering the fabrication parameters, such as the type of cellulose monolith and the amount of HA powder. Furthermore, bovine serum albumin (BSA) protein adsorption and release performance of the HA monolith were evaluated.

Results and discussion

Fig. 1a shows the preparation process of the HA monolith. The hierarchically porous cellulose monolith was fabricated according to the TIPS method reported in a previous study.[28] The cellulose_HA monolith was prepared by a reaction of HA slurry with the cellulose monolith. The cellulose monolith template and chitosan were then removed by burning at 900 °C to obtain the HA monolith. The cellulose_HA monolith retained a good columnar shape. By removing the cellulose, an HA monolith with a good columnar shape was prepared, despite a slight shrinkage compared to the cellulose_HA monolith (**Fig. 1a**). The porous structures of the cellulose, cellulose_HA, and HA monoliths were examined *via* SEM (**Fig. 1b**). Similar to the porous structure of the cellulose monolith, the obtained cellulose_HA and HA monoliths showed a porous structure. The macropore diameter of the cellulose80_HA2 monolith was 12.8 ± 3.1 μm, which was smaller than that of the cellulose80 monolith (15.2 ± 3.9 μm) as a template; the HA80_2 monolith (9.7 ± 1.7 μm) also showed a smaller macropore diameter after the removal of the template. The uniform distribution of HA in the cellulose template can also be proved by EDX mapping (**Fig. S1**). It can be clearly observed that P and Ca were uniform distributed in the monolith. The thermal decomposition behavior of the template between 40 and 900 °C was studied using TGA (**Fig. 3f**). The weight loss of cellulose and cellulose_HA monoliths commenced at 300 °C and stopped after 450 °C; however, the HA monolith did not show any weight loss. Therefore, a burning temperature of 900 °C was sufficient to remove the template.

The chemical structure of the monolith was studied *via* FT-IR, XRD, and X-ray photoelectron spectroscopic (XPS) analyses. As shown in **Fig. 1c**, in the FT-IR spectrum of the cellulose monolith, the bands at 1023, 2920, and ~3400 cm^{-1} were assigned to C-O-C, C-H, and the stretching vibration of O-H, respectively.[28] The characteristic peaks of HA powder observed at 1027 and 962 cm^{-1} were assigned to P-O, and peaks at 601 and 569 cm^{-1} were assigned to O-P-O.[30] The peaks of cellulose OH groups were weakened and shifted to lower wavenumbers in the presence of HA slurry. This result is related to intramolecular hydrogen bonding, indicating that the cellulose OH groups are bonded with the HA slurry. The formation of chemical bonds between cellulose and the HA slurry can stabilize the composite monoliths. XRD was performed to characterize the cellulose_HA composite monolith, as shown in **Fig. 1d**. XRD patterns of the HA powder display clearly typical characteristic peaks (002) (211), (300), (202), (310), (222), and (213) arising from crystalline HA phase according to the standard card of HAP (JCPDS files, PDF No. 09-0432). The cellulose monolith exhibited a peak at $2\theta = 20.3°$, while the cellulose_HA monolith showed all peaks of cellulose and HA powder, indicating that HA was successfully incorporated into the cellulose monolith, and after removal of the template, the HA monolith showed the same peaks as the HA powder. The XPS survey patterns of cellulose_HA indicate the presence of P and Ca compared to that of pure cellulose (**Fig. 1e**). The high-resolution scan XPS images of O 1s are shown in **Fig. 1f**, which can be deconvoluted into two peaks, i.e., those at binding energies of 530.5 and 532.0 eV, which can be attributed to the P–O and C–O bonds, respectively.[31]

Fig. 2 shows a schematic illustration of the preparation of the HA monolith. The cellulose_HA monolith was prepared by immersing the cellulose monolith into the HA slurry. The Ca ions and –OH groups of HA can interact with the $–NH_2$ or –OH groups of chitosan to form a homogenous HA slurry (HA-chitosan slurry);[29] therefore, the preparation process of the cellulose_HA monolith might be explained in terms of possible interactions between the OH groups of cellulose and HA slurry. The samples were then transferred to an oven at 80 °C overnight. During the drying process, with the evaporation of

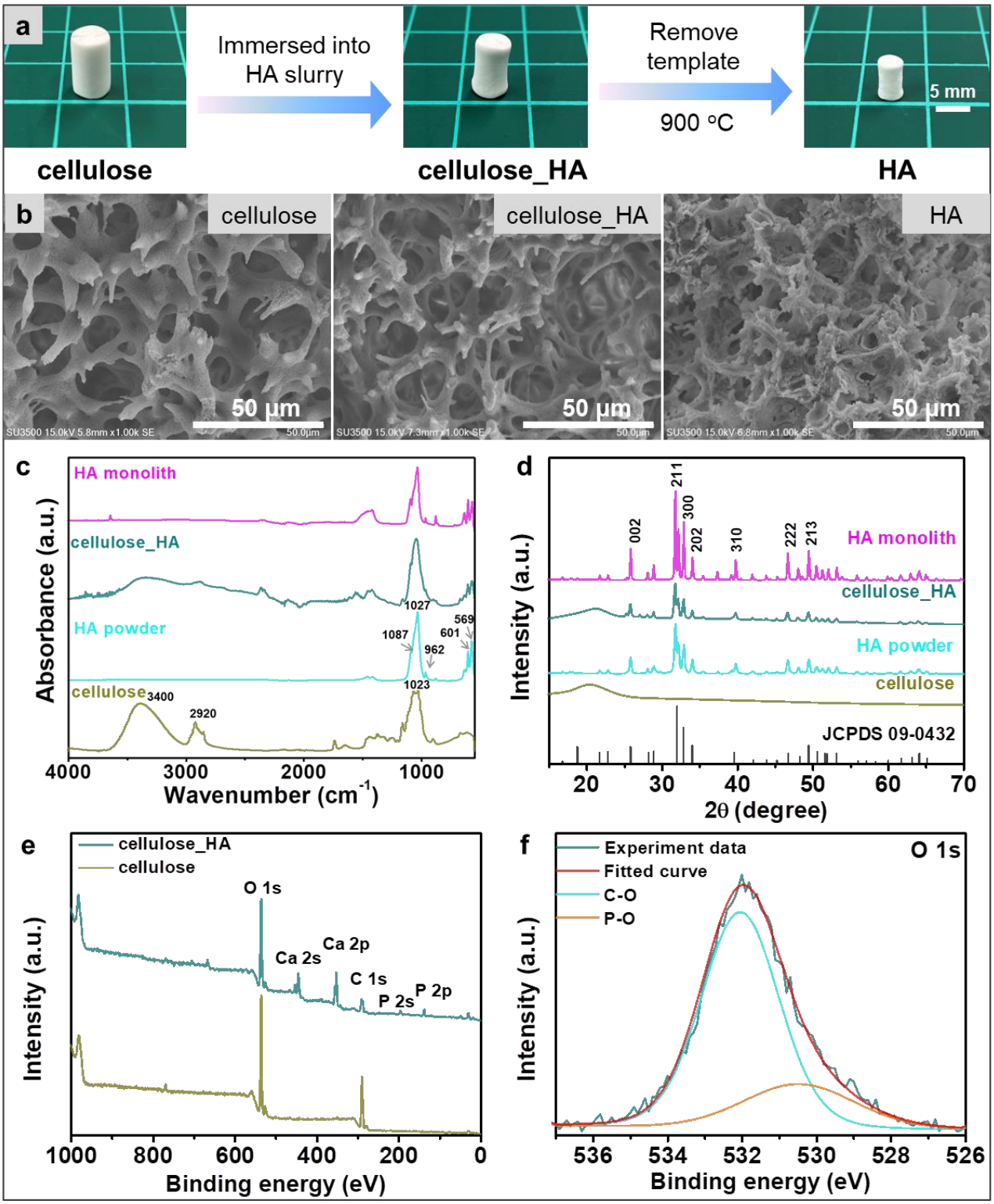

Fig. 1 (a) Preparation process of the HA monolith. (b) SEM images of the prepared cellulose80, cellulose80_HA2, and HA80_2 monoliths. (c) FT-IR spectra of HA powder, cellulose80, cellulose80_HA2 and HA80_2 monoliths, (d) XRD spectra of HA powder, cellulose80, cellulose80_HA2, HA80_2 monoliths and the standard card of HA (JCPDS 09-0432), (e) survey XPS images of cellulose80 and cellulose80_HA2. (f) High-resolution XPS images of O 1s of cellulose80_HA2.

the solvent and water, the volume of the filled HA slurry was reduced; thus, the vacancy uniformly appeared in the monolith. During solvent evaporation, the chitosan molecular chains shrunk. Because of the strong hydrogen bonding between chitosan molecular chains and HA powder, the shrinking of chitosan molecular chains dragged the HA, and it tightly stuck to the frame of the cellulose monolith. Thus, a uniform through-hole structure was formed in the cellulose monolith. The cellulose monolith template and chitosan were then removed by burning at 900 °C to obtain the HA monolith. During sintering,

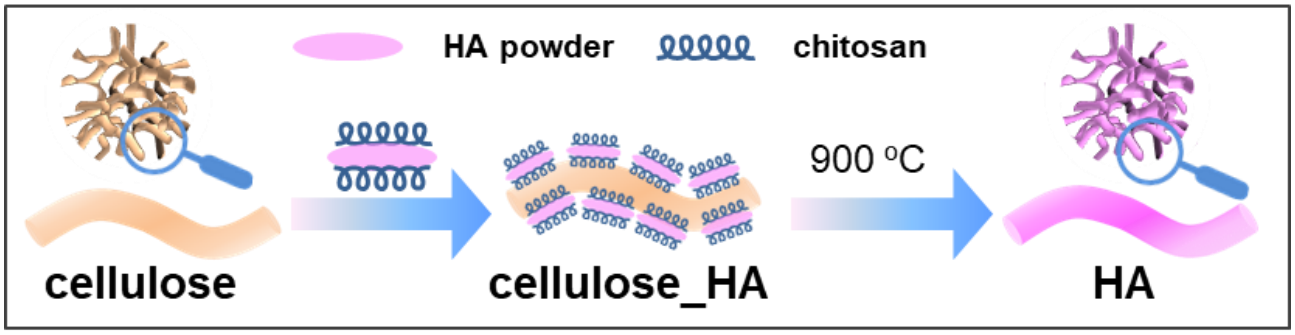

Fig. 2 Schematic illustration of the preparation of the HA monolith.

HA powder was sintered together and porous HA monolith was formed. Simultaneously, micropores formed on the through-hole structure because of the space occupied by HA.

As the amount of HA powder was considered to affect the amount of HA attached to the cellulose monolith, the macropore diameter of the cellulose_HA and HA monoliths was evaluated with different amounts of HA powder using the same template (cellulose80). During the calcination process, the HA powders were sintered together to form a porous HA monolith. When the amount of HA powder was less than 2 g, after calcination, the HA powders could also be sintered together to form a porous structure; however, it is not enough to form a columnar skeleton structure because the amount of HA powder covering the skeleton surface is not sufficient. As shown in **Fig. 3**, increasing the amount of HA powder tended to decrease the macropore diameter. The macropore diameters at each reaction stage were investigated, as shown in **Fig. 3e**. When the amount of HA powder was sufficiently high, the macropore diameter decreased because the amount of HA powder covering the skeleton surface increased. It can also be confirmed using TGA, as shown in **Fig. 3f**; with an increase in the amount of HA powder, after burning at 900 °C, the weight percent of the cellulose_HA monolith increased, indicating that the amount of HA powder attached to the cellulose monolith increased.

The polymer concentration, aging temperature, and solvent composition can control the pore diameter of the cellulose monolith when the cellulose acetate monolith is a precursor of

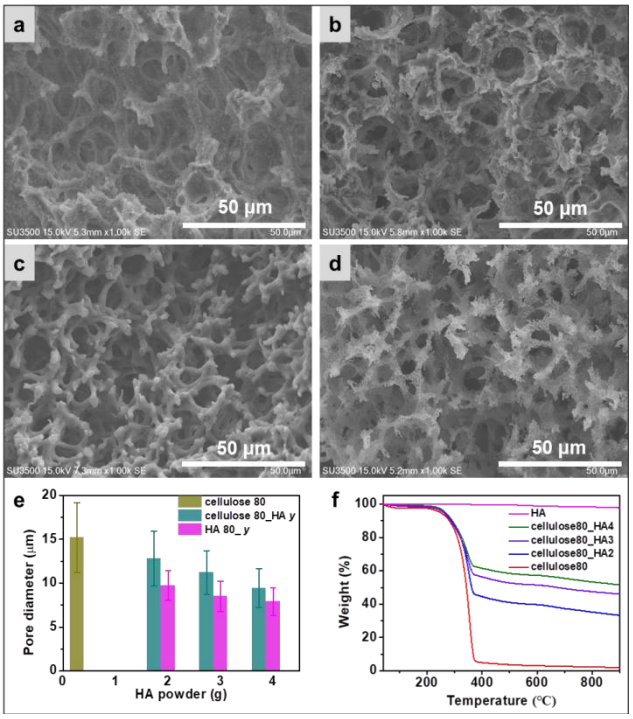

Fig. 3 SEM images of (a) cellulose80_HA3, (b) HA80_3, (c) cellulose80_HA4, and (d) HA80_4 monoliths. (e) Macropore diameter of cellulose, cellulose_HA, and HA monoliths prepared with different amounts of HA powders. (f) TGA of cellulose, cellulose_HA, and HA monoliths prepared with different amounts of HA powders.

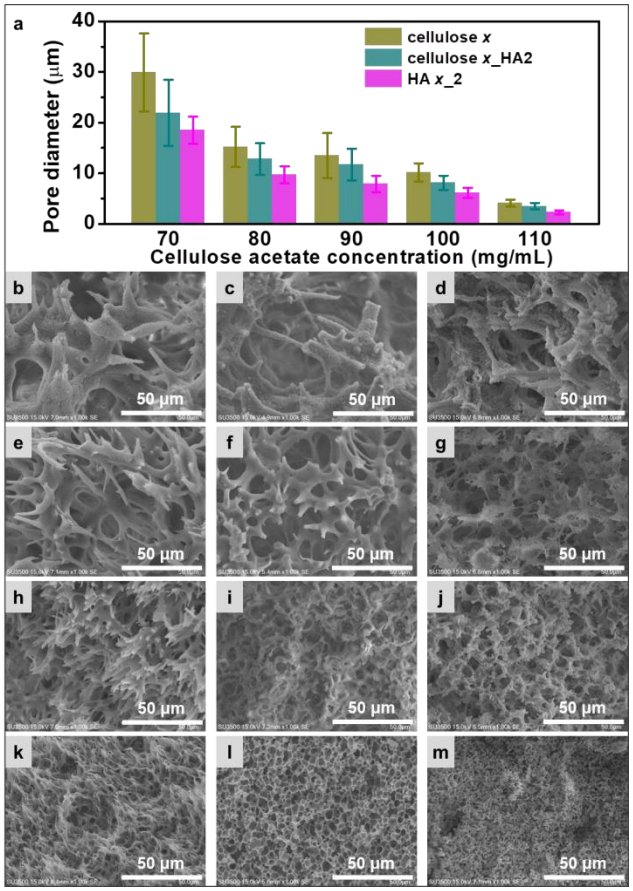

Fig. 4 (a) Macropore diameter of cellulose, cellulose_HA, and HA monoliths prepared with different cellulose acetate concentrations. SEM images of cellulose x monolith, cellulose x_HA2, and HA x_2 monolith. x is 70 for (b), (c), and (d); 90 for (e), (f), and (g); 100 for (h), (i), and (j); and 110 for (k), (l), and (m).

the cellulose monolith. Here, various HA monoliths with different pore diameters were prepared using a cellulose monolith template, which was obtained when the polymer concentration was changed.[28] The amount of HA powder was fixed at 2 g. As shown in **Fig. 4a**, with an increase in the cellulose acetate concentration, the macropore diameter of the cellulose monolith slightly decreased from 29.9 ± 7.7 μm (cellulose70) to 4.1 ± 0.7 μm (cellulose110); however, the obtained cellulose_HA monolith maintained the porous structure, and the HA monolith also reflected the template structure (**Fig. 4b–m**). These results indicate that the macropore diameter of the HA monolith can be controlled by changing the macropore diameter of the cellulose monolith template.

To evaluate the porous features of the HA monolith, nitrogen adsorption–desorption analysis was carried out; the isotherms and pore size distribution plots are shown in **Fig. 5a–b**. As shown in **Fig. 5a**, all curves can be classified as type IV with adsorption hysteresis loops in terms of the IUPAC classification, indicating the presence of mesopores.[32] The BET surface area, pore volume, and pore diameter are summarized in **Table 1**. The BET surface areas and pore volumes of cellulose80_HA2 were smaller than the template because HA powders entered the pores of cellulose and some pores closed. After removing the template, the BET surface areas and pore volumes of HA monolith was decreased. With an increase in the amount of HA powder or cellulose acetate concentration, the BET surface areas of all the HA monoliths were similar, the pore diameter decreased, and the pore volume increased slightly. Based on the pore diameter information obtained from the nitrogen adsorption–desorption analyses and SEM analysis, the HA monoliths had a broad pore diameter distribution (with abundant mesopores and macropores). Moreover, owing to the well-formed porous structure, the HA monoliths possessed a high porosity. As shown in **Fig. 5c–d**, with an increase in the amount of HA powder, the porosities of the HA80_*y* monoliths were similar (approximately 89.2–91.8%). With an increase in the cellulose acetate concentration, the porosity of the HA *x*_2 monoliths decreased slightly from 89.9% (HA70_2) to 80.6% (HA110_2).

For application as a column, liquid permeability of the solvent is required. Additionally, the absolute permeability was examined to determine the intensive properties of the monolith in the flow system. The monolith was mechanically strong enough to pass water during experiment. The permeability coefficient in the flow system, B_0, was measured at flow rates of 1, 2, 3, 4, and 5 mL/min, and then, was calculated using the average value. As shown in **Fig. 5c–d**, B_0 varied depending on the amount of HA powder and the type of cellulose monolith. With an increase in the amount of HA powder, the permeability of HA80_*y* monoliths decreased; with an increase in cellulose acetate concentration, the permeability of HA *x*_2 monoliths decreased.

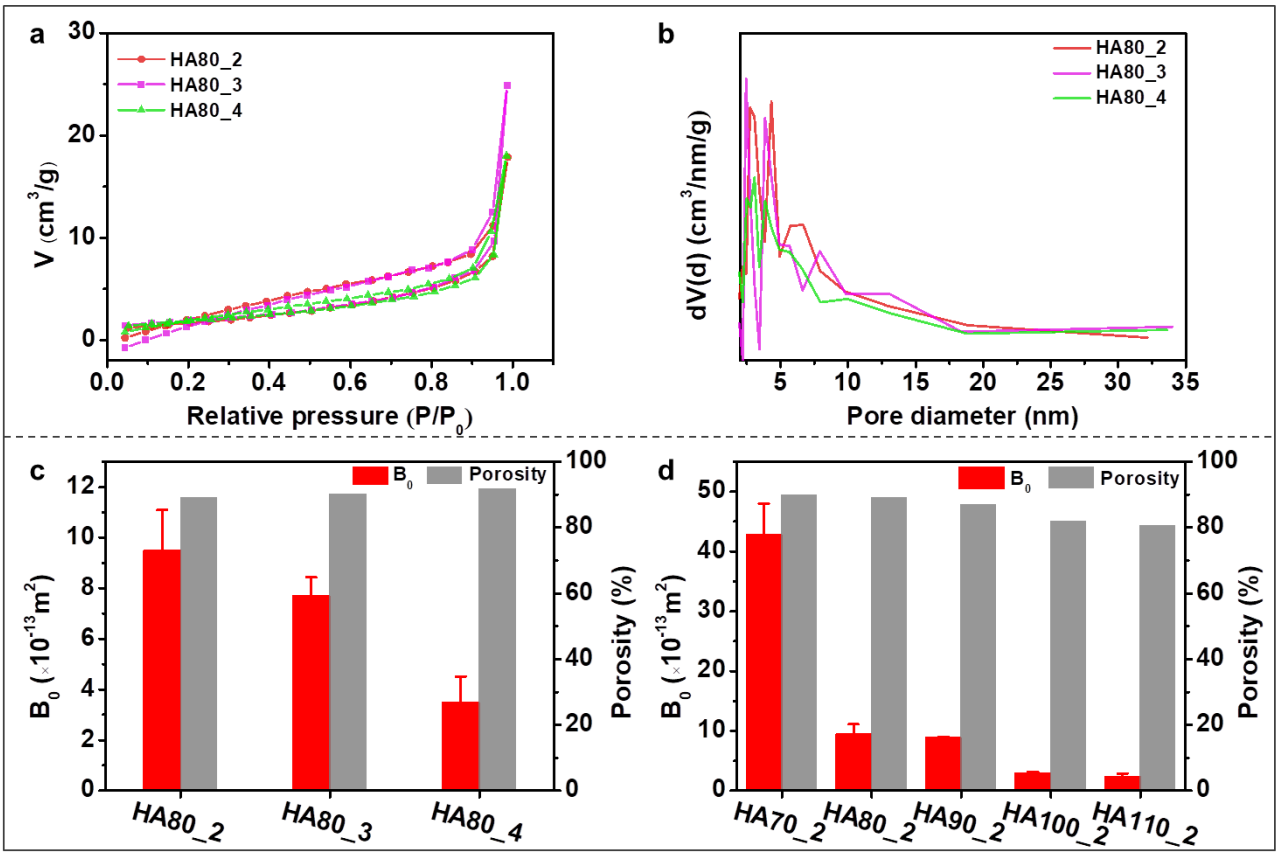

Fig. 5 (a) Nitrogen adsorption–desorption isotherm, (b) corresponding pore size distribution curve of the HA monoliths, permeability and porosity of (c) HA80_*y* and (d) HA *x*_2 monoliths.

Table 1 BET surface areas, pore volumes, and pore diameters of monoliths

Sample	Surface area (m^2/g)	Pore diameter (nm)	Pore volume (cm^3/g)
cellulose80	26.4	1.428	0.127
cellulose80_HA2	11.1	1.415	0.074
HA80_2	6.1	4.346	0.028
HA80_3	6.5	2.469	0.039
HA80_4	6.5	3.089	0.028
HA70_2	9.6	3.455	0.037
HA90_2	7.2	3.108	0.050
HA100_2	7.6	1.439	0.042
HA110_2	7.2	1.444	0.044

Table 2 Summary of the maximum BSA adsorption capacities of different adsorbents

Samples	qe (mg/g)	Flow system	References
CTA-HAp nanofibers	176.04	×	10
HA nanosheet	165	×	[33]
Cu^{2+} Cell/MHAP	101.7	×	[34]
SO_4^{2-} substituted nano-HA	55.8	×	[35]
HAp/GO nanocomposite	350	×	[36]
Poly(L-glutamic acid sodium salt)-HAp	98.5	×	[37]
HA monolith	388.6	√	This work

HA is a well-known effective adsorbent that can adsorb positively and negatively charged proteins, DNA, biological molecules, and heavy metal ions. Understanding the adsorption behavior of proteins is very important for determining their potential impact on biomedical applications. BSA was used as a model protein for adsorption studies. The adsorption capacity of the HA monolith for BSA was measured by varying the pH, initial concentration of BSA, and type of HA monolith.

In general, protein adsorption is attributed to electrostatic, van der Waals, and hydrophobic interactions due to the surface charges of the adsorbent. Hence, the electrostatic attraction between BSA and the HA monolith is the foremost function for surface adsorption. The electrostatic force was varied by altering the pH. The HA80_2 monolith was fixed in a PTFE heat-shrinkable tube and the BSA solution was allowed to flow circularly through the monolith using a peristaltic pump (**Fig. 6a**). **Fig. 6b** shows pH-dependent BSA adsorption capacity by the HA80_2 monolith in a pH range of 4.0–8.0 with an initial BSA concentration of 0.5 mg/mL at room temperature in a flow system. It shows that a maximum BSA adsorption capacity of 294.6 mg/g occurs at pH 6.0. Therefore, adsorption experiments were conducted at pH 6.0 and were suitable for all of our protein adsorption experiments.

Fig. 6c shows the effect of initial concentration (0.2–1.5 mg/mL) on the adsorption of BSA on the HA80_2 monolith for 120 min in PB solution at pH 6.0. The maximum BSA adsorption capacity was attained in the first 10 min. Then, the adsorption gradually increased with increasing contact time and reached saturation after 30 min. The BSA adsorption capacity on the HA monolith increased with increasing initial concentration in the range of 0.2–1.5 mg/mL and reached 388.6 mg/g at a BSA initial concentration of 1.5 mg/mL, which is higher than those reported for HA carriers.[33] These results clearly showed that the as-prepared HA monolith can be used as a good adsorbent material for the rapid adsorption of proteins. **Fig. 6d** shows that in the adsorption of BSA on the different HA monoliths for 120 min in PBS solution at pH 6.0 with an initial concentration of 0.5 mg/mL, all HA monoliths exhibited higher BSA adsorption capacity.

A comparison of the adsorption performance of our work with other HA adsorbents toward BSA found in the literature are given in **Table 2**. The results indicated that the as-prepared HA monolith exhibits higher adsorption performance than other HA adsorbents, and it can also be used in flow systems, while other samples cannot. In these studies, HA powders were meticulously supported on nanofibers or nanosheets and thus exhibited a relatively high adsorption performance. However, even compared with these works, our HA monolith exhibited higher adsorption performance and can be used in flow systems. Such a high adsorption performance can be attributed to the

highly interconnected three-dimensional hierarchical porous structures. The hierarchical macro/mesoporous structures of HA monolith can provide a large number of binding sites for protein molecules. Moreover, BSA can flow through more binding sites of HA which also can increase the adsorption performance in the flow system. Thus, HA monoliths can be used as good adsorbent materials for the rapid adsorption of proteins in a flow system.

The BSA release behavior of the HA monoliths was investigated at different pH values (6.0, 7.4, and 8.0) in PB solution at room temperature in the flow system (**Fig. 6a**). **Fig. 6e** depicts the cumulative release behavior of BSA loaded onto the HA monoliths. The pH-dependent cumulative release ratio (%) was determined by the amount of BSA released in the PB solution as a function of time. The BSA release rates were high during the first 150 min at different pH values. The cumulative BSA release percentage of BSA loaded on the HA monolith in PB solution at pH 6.0 reached 75.7% over 330 min. Additionally, cumulative BSA releases of 65.5% and 40.2% were obtained at pH 7.4 and 8.0, respectively.

The cumulative release percentage of BSA initially increased in the first 150 min at all pH values and reached a steady release until 330 min. The cumulative release profile confirmed the sustained release of adsorbed BSA on the HA monolith for 330

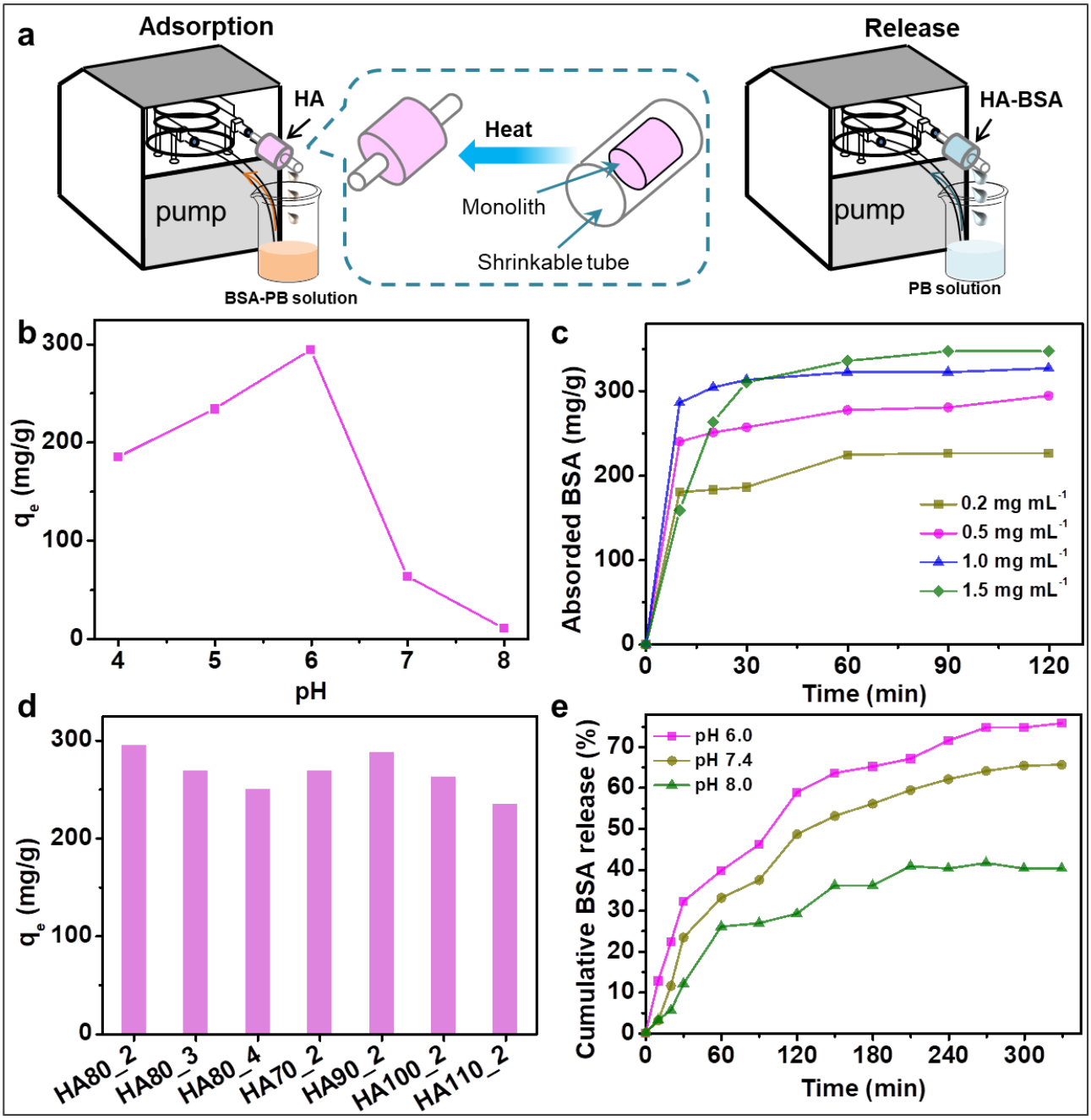

Fig. 6 (a) Schematic representation of the experimental setup used for protein adsorption and release. The effect of (b) pH value of BSA (initial concentration: 0.5 mg/mL) and (c) initial concentration of BSA (pH: 6.0) on the adsorption capacity for the HA80_2 monolith. (d) The BSA adsorption capacity for HA *x_y* monoliths (initial concentration: 0.5 mg/mL, pH: 6.0). (e) Cumulative release of BSA loaded on the HA80_2 in PB solution at room temperature.

min. The BSA release in PB solution at pH 6.0 was much larger than those at the other two pH values. The higher release rate and higher cumulative percentage of BSA released at a lower pH may be attributed to the diffusion of proteins entrapped near the surface and the maximum release of non-toxic calcium (Ca^{2+}) and phosphate (PO_4^{3-}) ions from the HA monoliths.[36] Compared with batch system, the flow system also can increase the release rate of BSA from the BSA-loaded HA monolith. These phenomena led to the rapid and sustained release of BSA from the BSA-loaded HA monolith. These protein release experiments confirmed that the HA monolith exhibited excellent protein adsorption and sustained release capacity of BSA.

Experimental

Materials

Cellulose acetate powder (CA, L30) with an acetylation degree of 55% was provided by Daicel Co., Ltd. Japan. Hydroxyapatite (HA) nanopowder (<200 nm particle size (BET), ≥97%, synthetic), isopropyl alcohol, and BSA were purchased from Sigma-Aldrich Co. LLC. Japan. All other chemicals were chemically purified and were commercially available.

Preparation of hydroxyapatite (HA) monolith

The cellulose monolith was prepared *via* the TIPS method reported in a previous study.[28] Cellulose acetate (1.75, 2.0, 2.25, 2.5, and 2.75 g) was dissolved in 10 mL dimethylformamide (DMF) at 90 °C. When the solution was completely dissolved by stirring, 15 mL of 1-hexanol was gradually added. After continuous stirring, the mixture became clear and was then transferred into a mold and kept at 20 °C for 6 h to induce phase separation to obtain the cellulose acetate monolith. The cellulose monolith was then obtained by deacetylation under alkaline conditions (0.5 mol/L NaOH in methanol) for 3 h. Finally, the dried cellulose monolith was obtained by vacuum drying. The cellulose monolith prepared with different concentrations of cellulose acetate was designated as cellulose *x* monolith, where *x* refers to the concentration of cellulose acetate.

The cellulose_HA monolith was prepared in the presence of a cellulose monolith. First, 200 µL of acetic acid was added to 10 mL of distilled water to dissolve chitosan, 0.3 g of chitosan powder was added to the aqueous acetic acid, and the mixture was stirred for 1 h. Then, different amounts of HA powder (2, 3, and 4 g) were added to the chitosan solution slowly and stirred for another 2 h to obtain a homogeneous HA slurry. Next, the cellulose monolith (0.2 g) was immersed in the HA slurry under stirring for 48 h. Then, the sample was washed with distilled water, following which the cellulose *x*_HA *y* monolith was obtained by drying in an oven at 80 °C overnight; *x* refers to the concentration of cellulose acetate (mg/mL), and *y* refers to the amount of HA powder (g). To remove the cellulose monolith, the cellulose_HA monolith was burned in air (increasing from 25 to 900 °C at a rate of 5 °C/min), maintained at 900 °C for 4 h, and then cooled to room temperature to prepare the HA *x_y* monolith.[6]

Characteristics

Fourier transform infrared (FT-IR) measurements of the samples were performed using a Thermo Scientific Nicolet iS5 spectrometer equipped with an iD5 ATR attachment. All spectra were acquired at a resolution of 4 cm^{-1} over 100 scans in the scan range of 500–4000 cm^{-1}. The morphology of the monoliths was investigated by scanning electron microscopy (SEM) using a Hitachi S-3000N scanning electron microscope operated at 15 kV. The Brunauer-Emmett-Teller (BET) surface area was studied by nitrogen adsorption–desorption analysis (Quantachrome Instruments). Samples were vacuum-degassed at 70 °C for 24 h prior to the measurement. The pore diameter distribution and pore volume were obtained using the Barrett-Joyner-Halenda (BJH) method. Thermogravimetric analysis (TGA) was conducted using a thermogravimetric analyzer (Hitachi, STA7200RV) in the temperature range of 40–900 °C at a heating rate of 10 °C/min under nitrogen protection. Powder X-ray diffraction (XRD) patterns were obtained using a SmartLab (In-plane) (Rigaku Corporation, Japan) using the Cu_K-beta mode at a scanning speed of 5°/min over a 2θ range of 5–70°. The generator voltage and current were 45 kV and 200 mA, respectively. Surface elemental composition was captured by Energy dispersive X-ray spectroscopy (EDX) (HITACHI, Miniscope TM 3000 equipped with Swift ED 3000).

To measure the permeability of the monolith, it was tightly fitted with a PTFE heat-shrinkable tube and was then connected to a digital quantitative tubing pump (As One, DSP-100SA) and a digital pressure gauge (Krone, KDM30). A peristaltic pump was employed to allow water to flow through the monolith. The value of the permeability coefficient, B_0, depends only on the structure of the porous medium. Hence, permeability is regarded as absolute regardless of the working fluid. Darcy's law defines the equation of permeability in terms of measurable quantities,[38]

$$\mathrm{B_0} = \frac{\mathrm{L} \times \mathrm{v} \times \mu}{\Delta \mathrm{P}}$$

$$\mathrm{v} = \frac{\mathrm{q}}{\mathrm{A}}$$

where L is the length of the monolith (m), v is the linear velocity of a given fluid in the flow system (m/s), μ is the viscosity of the fluid (Pa·s), Δ*P* is the pressure drop when influent flow through the monolith (Pa), q is the flow rate (m^3/s), A is the cross-sectional area of the flow (m^2), and B_0 is the permeability of the porous medium (m^2).

The porosity of the HA monoliths was evaluated by gravimetric measurements. The porosity was calculated using the following equation:

$$\text{porosity} = \left(1 - \frac{\rho_{\mathrm{ap}}}{\rho_{\mathrm{m}}}\right) \times 100\%$$

where ρ_m is the density of hydroxyapatite particles (ρ_m = 3.16 g/cm^3) and ρ_{ap} is the density of the prepared HA monolith.

Protein adsorption and release

BSA with an isoelectric point of 4.7 was taken as the model protein for the present investigation. The protein adsorption capacity of the HA monoliths was tested in a flow system at

room temperature. The HA monolith was fixed into a PTFE heat-shrinkable tube to construct a flow system, which was dissolved in a 0.01 mol/L phosphate buffer solution (PB solution), and the protein solution was flowed circularly through the monolith using a peristaltic pump (EYELA, MP-1000). The reservoir was filled with 20 mL of the protein solution, and the flow rate was set at 2 mL/min. The concentration of the protein solution was checked at different times using a UV-visible spectrophotometer (HITACHI, U-2810) at 280 nm to follow the adsorption of the protein solution. The effect of initial concentration (BSA solution: pH 6.0, c_0 = 0.2–1.5 mg/mL), pH values (BSA solution: pH 4.0–8.0, c_0 = 0.5 mg/mL), and different samples (BSA solution: pH 6.0, c_0 = 0.5 mg/mL) on the protein adsorption capacity of the HA monolith was studied. The experimental adsorption capacity for the protein was calculated using the following equation:

$$q_e = \frac{(c_0 - c_e)V}{m}$$

where q_e (mg/g) is the experimental adsorption capacity for protein, c_0 and c_e (mg/mL) are the initial and equilibrium protein concentrations, respectively, V (mL) is the volume of protein solution, and m (g) is the mass of the HA monolith.

The HA monoliths were dried overnight in an oven at 80 °C after the protein adsorption experiment. BSA-loaded dried HA monoliths were further used for the release study at different pH values (6.0, 7.4, and 8.0). The protein release of the HA monoliths was tested in a flow system at room temperature. The PB solution was circularly flowed through the monolith using a peristaltic pump. The reservoir was filled with 20 mL PB solution, and the flow rate was set to 2 mL/min. The concentration of the solution was checked at different times using a UV-visible spectrophotometer at 280 nm to monitor the release of protein solution.

Conclusions

A porous HA monolith was fabricated using a cellulose monolith as a template and commercial HA powder as the raw material. Owing to the hierarchically porous structure of the cellulose monolith template, the obtained HA monolith showed a similar hierarchically porous structure with a broad pore diameter distribution (with abundant mesopores and macropores). The pore structure was controlled by changing the cellulose acetate concentration and amount of HA powder. Furthermore, the HA monolith was explored to study the adsorption and release properties of BSA, and the results indicated that the HA monolith had a high adsorption capacity (388.6 mg/g) of BSA and exhibited a sustained release of BSA from the BSA-loaded HA monolith.

Conflicts of interest

There are no conflicts to declare.

Acknowledgements

This work was supported by JSPS KAKENHI Grants (No. 19H02778, No. 20H02797), and JST-Mirai Program (Grant No. JPMJMI18E3). Y. L. would like to thank China Scholarship Council (CSC) for a scholarship support.

Notes and references

1. L. C. Palmer, C. J. Newcomb, S. R. Kaltz, E. D. Spoerke and S. I. Stupp, *Chem. Rev.*, 2008, **108**, 4754-4783.
2. S. V. Dorozhkin, *Materials*, 2009, **2**, 399-498.
3. P. J. Shi, M. Liu, F. J. Fan, C. P. Yu, W. H. Lu and M. Du, *Mater. Sci. Eng. C*, 2018, **90**, 706-712.
4. S. Paul, A. Pal, A. R. Choudhury, S. Bodhak, V. K. Balla, A. Sinha and M. Das, *Ceram. Int.*, 2017, **43**, 15678-15684.
5. C. Shi, J. Y. Gao, M. Wang, Y. R. Shao, L. P. Wang, D. L. Wang and Y. C. Zhu, *Biomater. Sci.*, 2016, **4**, 699-710.
6. K. Zhou, P. Yu, X. J. Shi, T. X. Ling, W. N. Zeng, A. J. Chen, W. Yang and Z. K. Zhou, *ACS Nano*, 2019, **13**, 9595-9606.
7. S. C. Cox, J. A. Thornby, G. J. Gibbons, M. A. Williams and K. K. Mallick, *Mater. Sci. Eng. C*, 2015, **47**, 237-247.
8. N. K. Nga, N. T. T. Chau and P. H. Viet, *Colloids Surf. B*, 2018, **172**, 769-778.
9. Y. D. Yu, Y. J. Zhu, C. Qi and J. Wu, *Ceram. Int.*, 2017, **43**, 6511-6518.
10. T. Lan, Z. Q. Shao, J. Q. Wang and M. J. Gu, *Chem. Eng. J.*, 2015, **260**, 818-825.
11. F. Chen and Y. J. Zhu, *ACS Nano*, 2016, **10**, 11483-11495.
12. H. L. Oliveira, W. L. O. Da Rosa, C. E. Cuevas-Suarez, N. L. V. Carreno, A. F. da Silva, T. N. Guim, O. A. Dellagostin and E. Piva, *Calcif. Tissue Int.*, 2017, **101**, 341-354.
13. M. T. Raimondi, S. M. Eaton, M. Lagana, V. Aprile, M. M. Nava, G. Cerullo and R. Osellame, *Acta Biomater.*, 2013, **9**, 4579-4584.
14. F. Miculescu, A. Maidaniuc, S. I. Voicu, V. K. Thakur, G. E. Stan and L. T. Ciocan, *ACS Sustain. Chem. Eng.*, 2017, **5**, 8491-8512.
15. L. H. Fu, C. Qi, Y. J. Liu, W. T. Cao and M. G. Ma, *Sci. Rep.*, 2018, **8**, 8292.
16. A. Szczes, L. Holysz and E. Chibowski, *Adv. Colloid Interface Sci.*, 2017, **249**, 321-330.
17. S. Dutta, A. Bhaumik and K. C. W. Wu, *Energy Environ. Sci.*, 2014, **7**, 3574-3592.
18. J. Xiao, D. H. Mei, X. L. Li, W. Xu, D. Y. Wang, G. L. Graff, W. D. Bennett, Z. M. Nie, L. V. Saraf, I. A. Aksay, J. Liu and J. G. Zhang, *Nano Lett.*, 2011, **11**, 5071-5078.
19. Z. C. Wu, K. Tian, T. Huang, W. Hu, F. F. Xie, J. J. Wang, M. X. Su and L. Li, *ACS Appl. Mater. Interfaces*, 2018, **10**, 11108-11115.
20. T. Huang, Z. C. Wu, Q. Yu, D. G. Tan and L. Li, *Chem. Eng. J.*, 2019, **359**, 69-78.
21. Z. S. Liu, P. Jiang, G. Huang, X. W. Yan and X. F. Li, *Anal. Chem.*, 2019, **91**, 3659-3666.
22. H. R. R. Ramay and M. Zhang, *Biomaterials*, 2004, **25**, 5171-5180.
23. S. K. Hubadillah, M. H. D. Othman, Z. S. Tai, M. R. Jamalludin, N. K. Yusuf, A. Ahmad, M. A. Rahman, J. Jaafar, S. H. S. A. Kadir and Z. Harun, *Chem. Eng. J.*, 2020, **379**, 122396.
24. H. Bai, F. Walsh, B. Gludovatz, B. Delattre, C. L. Huang, Y. Chen, A. P. Tomsia and R. O. Ritchie, *Adv. Mater.*, 2016, **28**, 50-56.

25. S. Y. Chen, B. H. Zhou, W. L. Hu, W. Zhang, N. Yin and H. P. Wang, *Carbohydr. Polym.*, 2013, **92**, 1953-1959.
26. C. Busuioc, C. D. Ghitulica, A. Stoica, M. Stroescu, G. Voicu, V. Ionita, L. Averous and S. I. Jinga, *Ceram. Int.*, 2018, **44**, 9433-9441.
27. Z. T. Xie, T. A. Asoh and H. Uyama, *Carbohydr. Polym.*, 2019, **214**, 195-203.
28. Y. R. Xin, Q. C. Xiong, Q. H. Bai, M. Miyamoto, C. Li, Y. H. Shen and H. Uyama, *Carbohydr. Polym.*, 2017, **157**, 429-437.
29. X. M. Cheng, Y. B. Li, Y. Zuo, L. Zhang, J. D. Li and H. A. Wang, *Mat Sci Eng C-Bio S*, 2009, **29**, 29-35.
30. A. Yelten-Yilmaz and S. Yilmaz, *Ceram. Int.*, 2018, **44**, 9703-9710.
31. K. N. Li, J. N. Wang, X. Q. Liu, X. P. Xiong and H. Q. Liu, *Carbohydr. Polym.*, 2012, **90**, 1573-1581.
32. Z. Z. Li, B. Wang, X. M. Qin, Y. K. Wang, C. T. Liu, Q. Shao, N. Wang, J. X. Zhang, Z. K. Wang, C. Y. Shen and Z. H. Guo, *ACS Sustain. Chem. Eng.*, 2018, **6**, 13747-13755.
33. X. Y. Zhao, Y. J. Zhu, F. Chen, B. Q. Lu and J. Wu, *Crystengcomm*, 2013, **15**, 206-212.
34. K. F. Du, X. H. Liu, S. K. Li, L. Z. Qiao and H. Ai, *ACS Sustain. Chem. Eng.*, 2018, **6**, 11578-11586.
35. G. Radha, B. Venkatesan, S. N. Jaisankar, P. Rajashree and S. Balakumar, *Mater. Sci. Eng. C*, 2021, **120**, 111617.
36. G. Bharath, B. S. Latha, E. H. Alsharaeh, P. Prakash and N. Ponpandian, *Anal Methods*, 2017, **9**, 240-252.
37. S. Kojima, F. Nagata, S. Kugimiya and K. Kato, *Appl. Surf. Sci.*, 2018, **458**, 438-445.
38. G. W. Jackson and D. F. James, *Can. J, Chem. Eng.*, 1986, **64**, 364-374.